VOL. 26, NO. 9, SEPTEMBER 1989 J. AIRCRAFT 837

Numerical and Experimental Investigation of Isolated Propeller Wakes in Axial Flight

D. Favier,* A. Ettaouil,† and C. Maresca*
Université d'Aix-Marseille II, Marseille, France

Complementary numerical and experimental studies were used to investigate the isolated propeller aerodynamic field over a large range of operating parameters of the axial flight regime. The numerical approach is based on a free-wake-analysis calculation that uses a new complete equilibrium procedure for the wake divided into near and far regions. Measurements of instantaneous velocities, as well as overall thrust and torque, were performed to determine the wake geometry and the three-dimensional vortex flow streaming back from the propeller. A large check of the code efficiency to predict both overall and local aerodynamic quantities is realized through extensive comparisons with experimental data obtained on a model scale of a four-bladed propeller. From the present results, the code predictions are shown to be in good agreement with experiments for different axial flight conditions of the isolated propeller.

Nomenclature

A,B = tip vortex contraction coefficients defined in Eq. (1)
b = number of blades
c = local chord of the airfoil section, m
D,D_0 = propeller and hub diameters, $D = 0.85$ m; $D_0 = 0.14$ m
$H(r,\psi)$ = pitch of a vortex sheet filament defined in Eq. (9)
K_1,K_2 = tip vortex translation coefficients defined in Eqs. (2) and (3)
n = blade rotational frequency (rps)
$OXYZ$ = fixed coordinate system defined in Fig. 2
P = power of the propeller, $P = 2nQ$, W
R = propeller radius, $R = D/2$
r = radial distance from the axis of rotation, m
T,Q = thrust and torque of the propeller, N and N.m
t = time, s
U,V,W = velocity components defined in Fig. 2, m/s
V_∞ = freestream axial velocity, m/s
α_0 = mean pitch angle at $\xi = 0.70$
γ = operating parameter of the propeller, $\gamma = V_\infty/nD$
Γ = circulation on the blade or the wake, m^2/s
ξ = reduced blade radius, $\xi = r/R$
λ = advance ratio of the propeller, $\lambda = \gamma/\pi$
ψ = blade azimuth angle, deg
ψ_b = azimuthal periodicity, $\psi_b = 360$ deg/b, deg
ψ_s = azimuthal far wake position given by Eq. (5)
τ = thrust coefficient, $\tau = T/\rho n^2 D^4$
χ = power coefficient, $\chi = P/\rho n^3 D^5$
ω,Ω = angular rotational speed, $\omega = 2\pi n$, rad/s

Subscripts

t = relative to the tip vortex
VS = relative to the inboard vortex sheet

Superscript

$-$ = denotes quantity nondimensionalized by V_∞

Introduction

THE ability to predict local and overall blade airloads is nowadays of primary importance for providing and improving current rotary wing designs. Also, the capability to predict accurately the associated wake flow behind the rotating plane is required for the determination of aerodynamic interference effects on the aircraft components fixed wings and fuselage. This is especially true in the case of highly loaded propellers and tilted rotors recently proposed[1] for advanced transport aircraft.

Relative to the flowfield generated by isolated propellers and helicopter rotors operating in various flight regimes (hovering, axial, or forward flight), analytical models can be classified according to the way in which the vortical structures of the wake and their influence on the blade loading are modeled. Several earlier numerical investigations[2,3] have shown reasonable agreement with experiments when considering the problem of blade calculation by means of a prescribed wake-analysis method (PWA). In these models, the geometry of the wake and the vortical structures are prescribed, and induced velocities need to be calculated only at the different blade sections. The prescribed geometry is generally based on empirical modeling laws deduced from tests performed by using flow visualizations, hot-wire, and laser velocity measurement techniques.[4–7]

In order to improve the prediction accuracy of the free vortex-flow influence, several other investigators have proposed to include a free wake that is allowed to assume the geometry corresponding to the bound circulation distribution as determined by the inflow velocities and the blade configuration (planform, airfoil section, twist, tip shape, etc.). As a result, the solution procedure includes repeated changes of the wake geometry, until convergence is reached on bound circulation and thrust coefficient, and is, therefore, called a free-wake-analysis method (FWA); see Refs. 8–11 for examples. These FWA models use either lifting surfaces[8] or lifting lines[9,10] for the blade-loading distribution, and straight or curved vortex elements[11] for the wake-distortion influence. Convergent procedures have been realized for given thrust coefficient or for experimentally prescribed blade calculations.[12] In recent studies,[13–15] the FWA approach also appears as a very important and powerful tool to investigate the detailed aerodynamic behavior of rotary wings.

Based on the previous literature review, it can be deduced that the comparisons between FWA calculation results and available experimental data indicate good agreement in some

---

Received Feb. 20, 1988; revision received Oct. 1, 1988.

*CNRS Senior Research Scientist, Institut de Mécanique des Fluides. Member AIAA.

†Graduate Student, Institut de Mécanique des Fluides.

flight regimes and large deviations in others, especially for blades with nonlinear twists and/or sharp evolutive tip shapes, which are, nevertheless, of high importance for new aircraft design. As emphasized by several authors,[12-14] the major reasons of these discrepancies are due, to a large extent, to a still inadequate modeling of important parameters that characterize the vortex flow generated by a given blade configuration at a proper flight regime. A few examples of these parameters are 1) the accurate modeling of the initial wake geometry and especially the far wake region, which appears to have more critical influence in hover and axial regimes than in forward flight[13,14]; 2) the evolution of the tip vortex size and strength along its path in the near wake, which significantly affects the circulation distribution near the tip region[15,16]; and 3) the effects of blade-vortex interactions, which can introduce severe local azimuthal and spanwise gradients in the blade airloads.[17,18]

Additionally, although being a useful tool, the convergence of FWA calculation can be a very time-consuming process, especially with unconventional blade geometries and twists when no initial conditions exist for estimating the wake shape. The wake-equilibrium condition is, therefore, only realized on the tip vortex filament in most current FWA procedures (see Refs. 9–11). Moreover, probably due to the lack of a unified body of available test data, the validation of codes is generally made by means of limited comparisons with either overall airloads data or local wake measurements, except for a very few studies based on both.

The purpose of the present investigation is to address some of the points previously raised, and to present some recent results involving an application of the FWA technique to the axial flight regime of a four-bladed propeller with evolutive chord distribution and nonlinearly twisted blades.

Three objectives are pursued in the following sections. The first is to provide an accurate experimental modeling of the near and far wake associated with a large range of blade pitch angles α_0 and operating parameters γ of the isolated propeller. Extensive measurements of overall thrust and torque coefficients, as well as instantaneous three-dimensional velocities, are performed at several distances aft of the rotating plane to constitute a reliable data base for evaluating the calculation code efficiency. The second objective is to develop an efficient FWA method based on the complete wake-equilibrium procedure, e.g., on the tip vortex line as well as on the inboard vortex sheet filaments. The third objective is focused on checking the FWA method consistency and on evaluating its efficiency to predict both overall and local aerodynamic quantities characteristic of the axial flight regime.

Experimental Study and Wake Modeling

The experiments were conducted on a model scale of a propeller mounted in the open chamber of the S1 subsonic wind tunnel (elliptical test section: 3.3 × 2.2 m^2; length of the open chamber: 3 m; freestream velocity: 5 m/s $\leq V_\infty \leq$ 50 m/s). A front view photograph showing the model mounted in the open chamber is presented in Fig. 1.

This model consists of a four-bladed propeller of $D = 0.85$-m diam (hub diameter: $D_0 = 0.14$ m), driven by a 40-kW variable-speed motor and held vertically in the test section by means of a supporting mast (see Fig. 1). The angular rotational frequency and the blade tip speed can be varied within the ranges 140 rad/s $\leq \omega \leq$ 280 rad/s and, therefore, 60 m/s $\leq \omega R \leq$ 120 m/s.

The blades are constituted by the NACA 64A408 airfoil series with a nonlinear twist law defined in Table 1. The dimensional and design characteristics of this blade (thickness t/c, chord c/R, camber c_b) are also given in Table 1 as function of the blade radius $\xi = r/R$.

The present experimental approach involved a variety of measurement techniques suited for surveying the flow in the near- and far-wake regions and around the blades. The details of measurement procedures and data-reduction methods, including X-wire anemometry, two-dimensional laser velocimetry, flow visualizations, and strain-gauge techniques can be found in Refs. 6, 7, 10, and 12 for application to rotor and propeller studies. Here, only a brief description for the reader's convenience is given.

Airloads measurements (averaged thrust and torque) are made by means of strain-gauge cells mounted on the supporting mast of the model. The thrust τ and torque χ coefficients have been determined[6,16] over a large range of operating parameters ranging from zero thrust level to the stall domain.

The three-dimensional instantaneous velocity is measured using an X-wire probe displaced behind the rotating plane along radial and axial coordinates (r,Z) by means of an

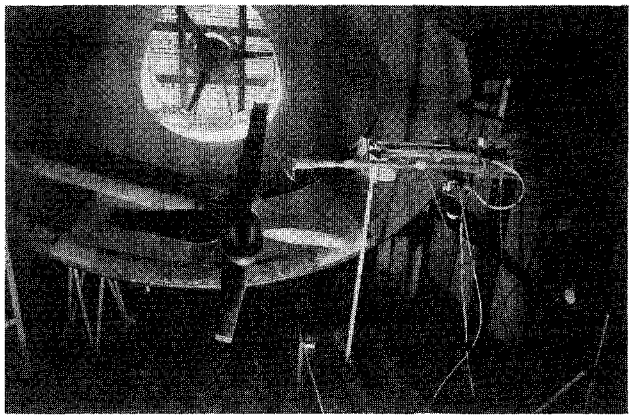

Fig. 1 View of propeller model and probe traversing device.

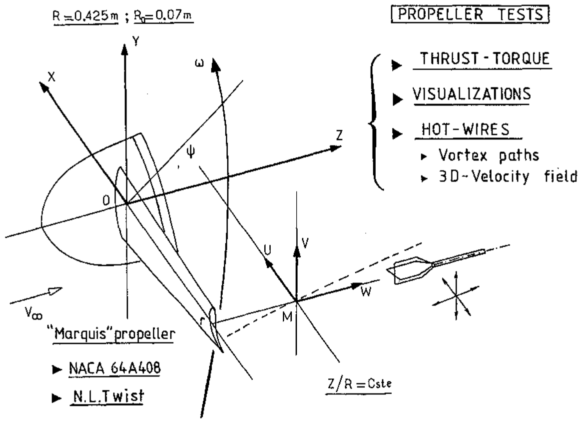

Fig. 2 Wake referential system and U,V,W velocity components.

Table 1 Propeller blade elements details

ξ	0.176	0.300	0.400	0.500	0.600	0.700	0.800	0.900	1.000
t/c	0.187	0.091	0.085	0.082	0.080	0.073	0.052	0.051	0.051
c/R	0.205	0.292	0.280	0.242	0.203	0.174	0.155	0.143	0.134
c_b	0.40	0.40	0.40	0.40	0.40	0.35	0.30	0.20	0.15
θ_t deg	28.3	20.8	25.1	9.66	4.53	0.00	−4.5	−8.3	−11.5

automated traversing mechanism shown in Fig. 1. The velocity components U,V and the redundant axial component W are determined in the fixed reference system defined in Fig. 2. Because of evolutive blade-chord distribution, the velocity measurements cannot be made closer than $Z/R = 0.20$ aft of the rotating plane. At any given measuring point in the wake, a large amount of azimuthal-dependent data is stored and processed through a data-acquisition and reduction system (Intertechnique IN 110 and HP 9845 B computer) to obtain each velocity component U,V,W as a function of the rotational azimuth varying in the range $0 \text{ deg} \leq \psi \leq 90 \text{ deg}$ (for the present four-bladed propeller). The initiation and synchronization of the data acquisition are achieved by means of a photoelectric cell delivering the azimuthal origin ($\psi = 0$ deg) at the blade passage in front of the fixed measuring point in the absolute reference frame. In order to constitute a reliable data base on the three-dimensional velocity field synthesized by Fourier series, several distances aft of the rotating plane ($0.2 \leq Z/R \leq 2.0$) have been investigated for seven values of the operating parameter ($0.2 \leq \gamma \leq 1.1$) and five different pitch angles ($23 \text{ deg} \leq \alpha_0 \leq 32.5 \text{ deg}$). An example of the three-dimensional instantaneous velocity field $\bar{U},\bar{V},\bar{W}$ (nondimensionalized by V_∞) is presented in Figs. 3a–3c for $\alpha_0 = 32.5$ deg, $\gamma = 0.89$, $Z/R = 0.203$, and at 15 different radial stations ($0.2 \leq \xi \leq 1.0$). As shown in these plots, the tip vortex passage through the fixed downstream plane $Z/R = 0.203$ is responsible for the significant disturbances observed in each component ($\bar{V}$ and $\bar{W}$ are maximum and $U = 0$). The smaller inboard disturbances observed in the plots are a result of the blade wake and of the hub vortex influence.

Tip vortex paths (r_t, Z_t, ψ_t) are measured by two complementary techniques based on flow visualization and hot-wire probing. The flow visualization consists of emitting white smoke filaments upstream of the rotating plane to reveal the vortex-structure development very close to the blade. A strobe flash synchronized on the blade rotation lights up the emission lines, which are filmed by a video camera and recorded on a magnetoscope tape. For $\alpha_0 = 27$ deg and $\gamma = 0.71$, the photographs in Fig. 4 give an example of the vortex structures, visualized at a fixed azimuth ($\psi = 0$ deg), and shed from the blade when varying the smoke emission from the tip towards the inboard sections ($0.7 \leq \xi \leq 1$). From such records repeated at different azimuths of the period, the pseudohelicoidal paths of the vortex lines are then obtained as a function of the blade radius ξ. Additionally, this visualization method provides useful data on the growth of the vortex core as a function of its age (see Fig. 4).

However, the smoke diffusion renders the visualization method inadequate for the accurate survey of the middle and far-wake regions. In those regions, a hot-wire technique based on the localization in space and time of the tip vortex center (corresponding to $\bar{U} = 0$ and $\bar{W}$ maximum as illustrated in Figs. 3a–3c). This hot-wire technique additionally allows the determination of the far-wake position where space–time instabilities of the tip vortex start to develop. The beginning of the far wake is defined by the azimuthal position ψ_s where instabilities are initiated. Beyond the azimuth ψ_s, the vortex instabilities gradually increase and the pseudohelicoidal form of the path is destroyed when going further back in the wake due to viscous dissipation and vortex interaction.

An example of the tip vortex paths $r_t/R = r_t/R(\psi)$ and $Z_t/R = r_t/R(\psi)$ measured by hot-wire probing at $\alpha_0 = 27$ deg and for 7 different operating parameters ($0.3 \leq \gamma \leq 1.0$) is given in Figs. 5a and 5b; also shown in the figure are the results deduced from the flow-visualization method implemented in the region close to the blade ($\psi < 45$ deg), as well as the results obtained on the far-wake localization (dotted line) indicated by the azimuth ψ_s where tip vortex instabilities are initiated.

From extensive tests conducted over a wide range of the axial flight regime parameters ($23 \text{ deg} \leq \alpha_0 \leq 32.5 \text{ deg}$ and $0.2 \leq \gamma \leq 1.1$), the vortex contraction and convection (r_t,Z_t) have been synthesized according to the following fitting laws:

$$r_t/R = A + (1 - A)e^{-\psi/B} \qquad \text{for } 0 \leq \psi \leq \psi_s \qquad (1)$$

$$Z_t/R = K_1(\psi/\psi_b) \qquad \text{for } 0 \leq \psi \leq \psi_b \qquad (2)$$

$$Z_t/R = K_1 + K_2(\psi/\psi_b - 1) \qquad \text{for } \psi_b \leq \psi \leq \psi_s \qquad (3)$$

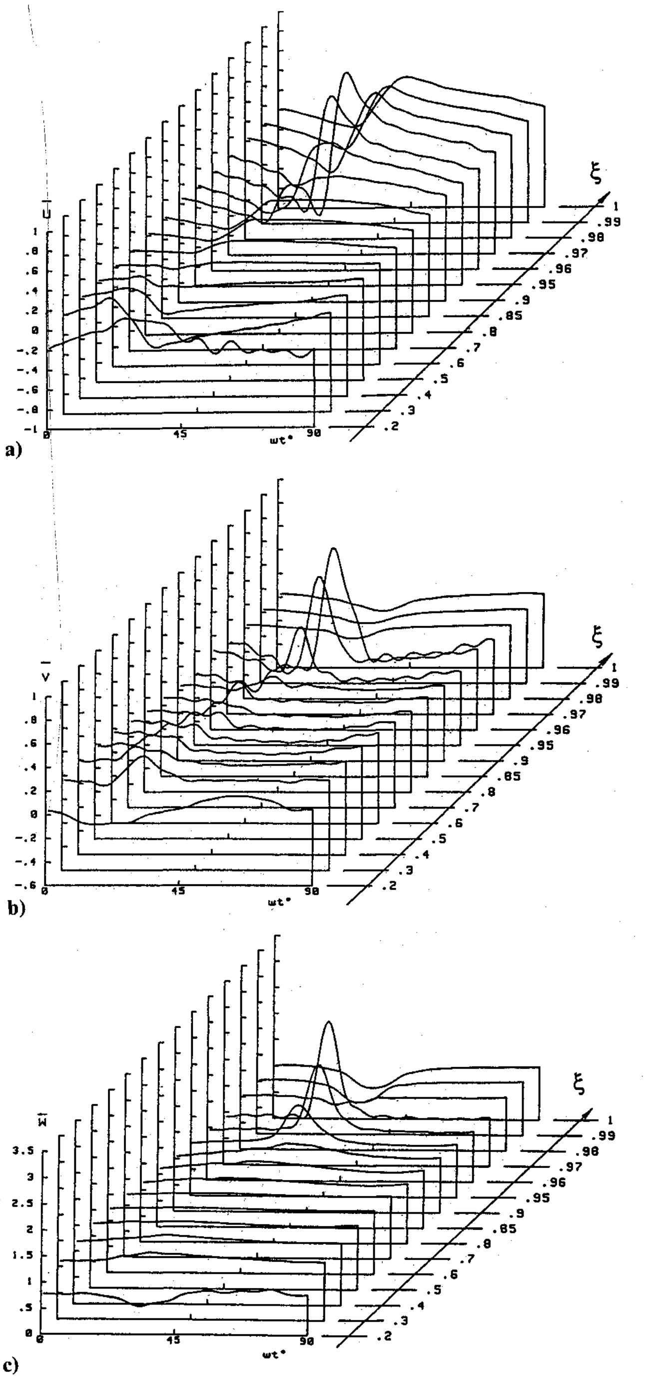

α_0	=	32.5°
γ	=	0.89
Z/R	=	0.203

Fig. 3 Three-dimensional instantaneous velocity field vs ψ for $Z/R = 0.203$ and as a function ξ, $\alpha_0 = 32.5$ deg and $\gamma = 0.89$: a) $\bar{U}$ component; b) $\bar{V}$ component; and c) $\bar{W}$ component.

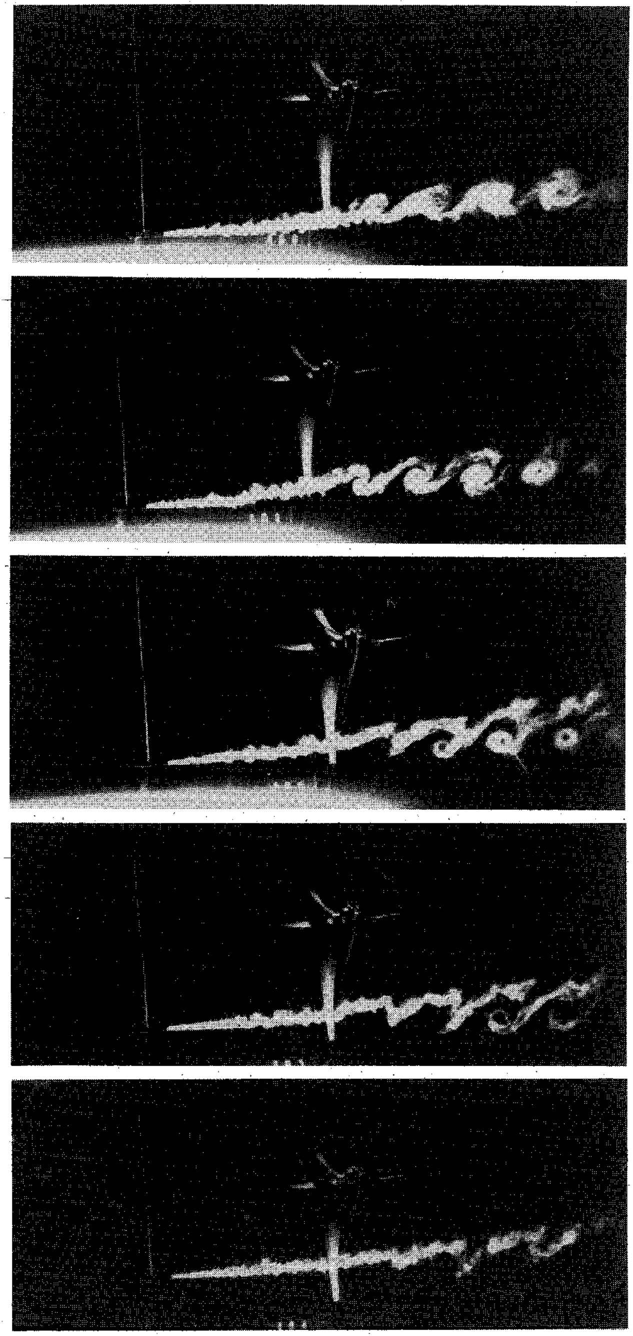

Fig. 4 Visualizations of vortex structures development as a function of ξ at $\psi = 0$ deg, and for $\alpha_0 = 27$ deg and $\gamma = 0.71$.

with A, B, K_1, and K_2 defined as

$$A(\alpha_0, \gamma) = P_A(\gamma) + \alpha_0 Q_A(\gamma) \qquad B(\alpha_0, \gamma) = P_B(\gamma) + \alpha_0 Q_B(\gamma) \quad (4)$$

$$K_1 = Z_0 + Z_1 L + Z_3 L^3$$

$$K_2 = Z'_0 + Z'_1 L + Z'_2 L^2 + Z'_3 L^3$$

where the coefficients (P_A, Q_A) and (P_B, Q_B) are expressed as second-order polynomial expressions of γ^2, and coefficients (Z_i), $0 \leq i \leq 3$, and (Z'_i), $0 \leq i \leq 3$, are expressed as polynomial expressions of second order in α_0 and first order in γ. Numerical values for all of the above coefficients can be found in Refs. 6 and 16. The L-parameter is defined as $L = \lambda / \lambda_T = \gamma / \gamma_T$, where λ_T and γ_T correspond to the zero-thrust coefficient conditions.

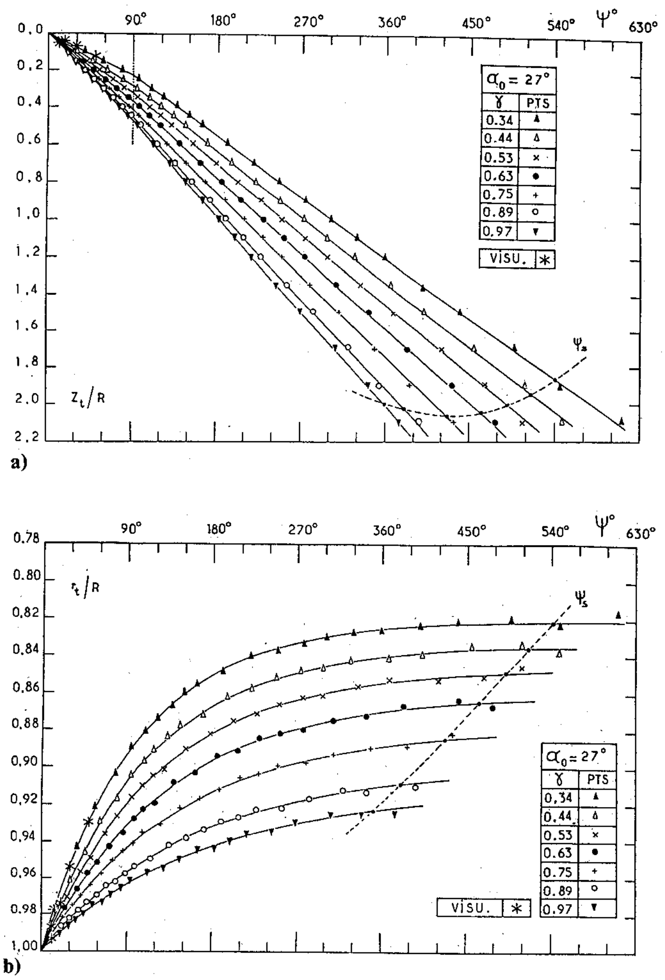

Fig. 5 Empirical tip vortex paths modeling at $\alpha_0 = 27$ deg, "———" empirical formulation from Eqs. (2–4); "– – –" far-wake position from Eq. (5): a) axial convection $Z_t/R = Z_t/R(\psi,\gamma)$; and b) radial contraction $r_t/R = r_t/R(\psi,\gamma)$.

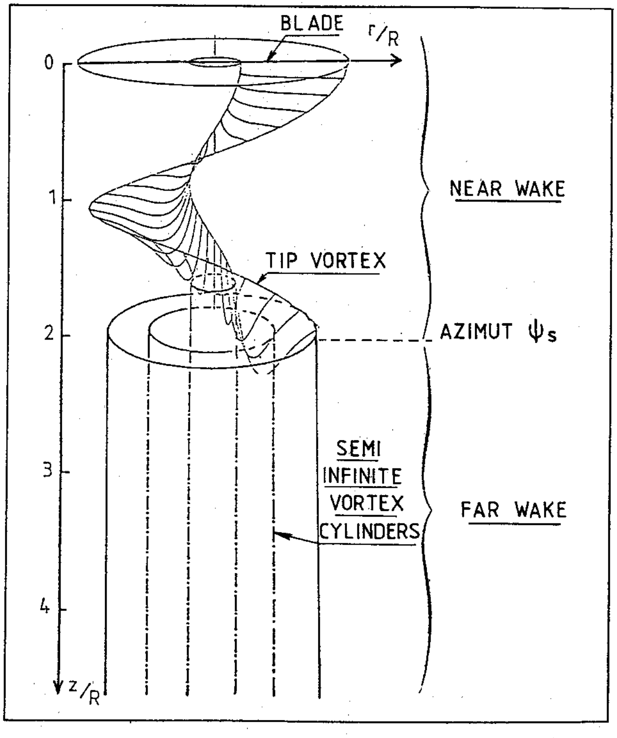

Fig. 6 Far-wake modeling by semi-infinite vortex cylinders.

In the Eqs. (2–4), the azimuth ψ is expressed in degrees and ψ_b only represents an azimuthal periodicity ($\psi_b = 360$ deg/b). The azimuthal position ψ_s of the far-wake region has been also synthesized as

$$(\psi_s - \psi_b)/b\psi_b = 1/4[8.5 - \alpha_0/10 - \gamma(2+\gamma)] \qquad (5)$$

In Figs. 5a and 5b, the preceding empirical-fitting laws are represented by full lines and the beginning of the far-wake region by dotted lines. It is worth noting that similar forms of the r_t and Z_t tip vortex coordinates are obtained for either the hovering rotor case[2,3] or the present axial flight propeller case. However, emphasis should be placed on the fact that coefficients (A,B) and (K_1,K_2) of Eqs. (1–3) are strongly dependent on the upstream conditions (α_0,γ) for the present propeller wake.

FWA Calculation Model

The derivation of basic equations and the blade and wake representations used in the present FWA approach are similar to those previously developed for the hovering rotor case.[10,12,16] Only the new features introduced in this approach are described here, e.g., the complete equilibrium procedure, the far-wake modeling, and the associated main code operations. More details on the resolution technique used for the present equilibrium procedure can be found in Ref. 19.

Each blade is considered as a lifting line spanning the quarter-chord airfoil sections and is divided into a finite number of vortex segments. The bound vorticity is continuously distributed along the lifting line and is represented by a finite sum of sine terms along the blade span. The N_P blade calculation points are located in the middle of each vortex segment. Because the bound circulation gradient $\mathrm{d}\Gamma/\mathrm{d}r$ appears to be higher near the blade ends, the number of calculation points has been increased towards the hub and towards the tip. Eleven control points usually have been used for the present calculations.

A number of trailing vortex filaments $N_L = N_P + 1$ leave every blade and form the wake, which is divided into near and far regions. The near region starts at the trailing edge of all of the blades and ends at the azimuthal distance ψ_s behind it. In the near region, the operating mode consists in dividing the blade wake in a rolled-up tip vortex line and in several trailing vortex lines constituting the inboard vortex sheet. Given the upstream operating conditions (α_0,γ) of the propeller, the tip vortex line (r_t,Z_t) and the far-wake position ψ_s are, therefore, known from the synthesized Eqs. (1–5).

Then, for each vortex line $(i = 1,2,\ldots,N_L)$ of the inboard vortex sheet, it is assumed that the radial $r^i_{VS}(r,\psi)$ and the axial $Z^i_{VS}(r,\psi)$ coordinates are expressed in the form

$$r^i_{VS}/R = \xi r_t(\psi) \qquad \text{for } 0 \le \psi \le \psi_s \qquad (6)$$

$$Z^i_{VS}/R = H(r,0)\psi \qquad \text{for } 0 \le \psi \le \psi_b \qquad (7)$$

$$Z^i_{VS}/R = H(r,0)\psi_b + H(r,\psi_b)(\psi - \psi_b) \qquad \text{for } \psi_b \le \psi \le \psi_s \qquad (8)$$

where the two functions $H(r,0)$ and $H(r,\psi_b)$ depend on the coordinates of the vortex filaments at the emission ($\psi = 0$) and at the azimuth $\psi = \psi_b$ in the wake. At any point, they can be expressed as a function of the induced velocities U,V,W, and azimuth ψ as

$$H(U,V,W,\psi) = (\pi/180)(V_\infty + W)/[\Omega + (U\cos\psi - V\sin\psi)/r] \qquad (9)$$

Equation (9) means that each filament of the inboard vortex sheet has a radial contraction proportional to that of the tip vortex and depends on the emission point on the blade [Eq. (6)]. Moreover, the pitch $H = H(r,\psi)$ of this helical vortex filament is determined by the induced velocities calculated at $\psi = 0$ and at $\psi = \psi_b$[Eqs. (7–9)].

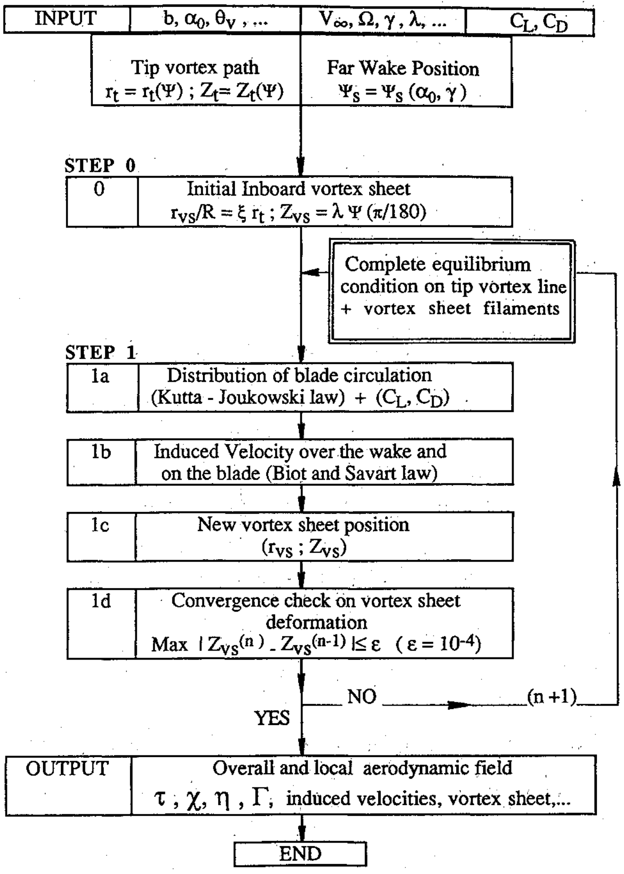

Fig. 7 FWA block diagram for complete equilibrium procedure.

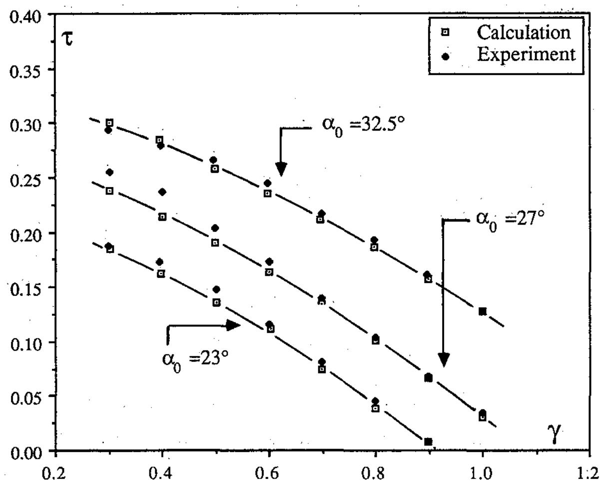

Fig. 8 Comparison of calculation and experiment on the thrust coefficient $\tau = \tau(\gamma)$.

Concerning the far-wake region, it starts at the azimuth ψ_s given by Eq. (5) and is composed of N_L semi-infinite vortex cylinders as shown in Fig. 6. Each cylinder is composed of an infinite number of rings having a constant vorticity $(-\mathrm{d}\Gamma/\mathrm{d}r)$ and a constant radius. The radius of each cylinder is equal to that of the corresponding vortex filament in the near wake. The velocity field induced by the far wake at any point on the blade or in the near wake is then calculated by using the Biot and Savart law. It can be noticed that only one vortex cylinder (associated to the tip vortex line alone) was introduced in previous FWA models[12,16] on hovering rotors to account for the far-wake region influence. As it will be shown in the following results the use of several vortex cylinders has the effect of significantly improving the three-dimensional velocity field prediction along the blade radius direction. Moreover, in order to avoid singularity problems a finite-vortex core model similar to the classical Rankine model has been applied. As deduced from flow visualizations and hot-wire surveys, a vortex core radius of about $0.01R$ has been used[19] in the present model.

From these blade and wake representations, the solution procedure is summarized in the block diagram shown in Fig. 7. The input data of the model are the geometrical configuration and the upstream operation conditions of the propeller: the number of blades b, the blade geometry characteristics (mean pitch angle α_0, twist and chord distributions, etc.), the freestream axial velocity, the angular rotational speed Ω, and the advance ratio $\lambda = \gamma/\pi$. Also given are the airfoil section characteristics (C_L, C_D) represented in standard tabular form as functions of angle of attack and Mach number. The tip vortex coordinates (r_t, Z_t) and the azimuthal far-wake position ψ_b are then deduced from the empirical synthesized Eqs. (1–5).

Then an initial position of the inboard vortex sheet is assumed (step 0 in Fig. 7). This initial position is deduced from Eqs. (6–8) and assuming that the pitch of the vortex sheet equals the advancing parameter, e.g., $Z_{rs}/R = \lambda\psi(\pi/180)$.

Now the FWA procedure consists of calculating a new vortex sheet position (steps 1a–1d in Fig. 7) as deduced from the induced velocity field and the bound circulation established along the blade radius. Then the sequence is repeated until the calculated velocity field becomes tangent at every calculation point of each vortex line (e.g., the tip vortex as well as the vortex sheet filaments), in order to realize the complete equilibrium condition. The iterating procedure stops when the vortex-sheet deformation becomes negligible between two iterating steps $n-1$ and n: e.g., $\max|Z_{VS}{}^{(n-1)} - Z_{VS}{}^{(n)}| < \varepsilon$ with $\varepsilon = 10^{-4}$. When the converged solution is obtained and the equilibrium condition is satisfied, all of the overall propeller performances (τ, χ, η) and the local aerodynamic quantities (velocity field, circulation distribution, vortex-sheet position) are obtained as model outputs.

It can also be noticed that the complete equilibrium procedure described previously for the present axial flight propeller configuration is not much more demanding in computing time than the FWA models previously developed for the hovering rotor case[12,16] (although in this last case the equilibrium condition was only satisfied on the tip vortex line). As an example, 3 min CPU time (IBM 3081) is required for calculation of the complete aerodynamic propeller field at a given pair of operating parameters (α_0, γ). The same computing time was required in the same conditions for the FWA calculation on a four-bladed hovering rotor at a given thrust coefficient (see Refs. 12 and 16). Additionally, a pitch angle change (of about 1 deg) was required to converge the FWA procedure and to match the thrust coefficient of the hovering rotor, while the initial pitch-angle value α_0 is strictly conserved during the present equilibrium procedure on the advancing propeller.

Results and Discussion

As indicated above, one of the objectives here is to check the consistency of the FWA method by comparisons with experimental data obtained on both the overall and local aerodynamic fields of the propeller.

Concerning the overall propeller performances, the Figs. 8 and 9 present the calculated and measured results on the thrust and power coefficients (τ, χ) obtained at increasing values of the mean pitch angle α_0 of 23, 27, and 32.5 deg. In the plots of Fig. 8, the calculated thrust coefficient τ exhibits a good agreement with experiments when the operating parameter is increasing from $\gamma = 0.3$ to $\gamma = 1.0$, and for three values of α_0. As an example, when considering the three operating conditions [$(\alpha_0 = 23$ deg, $\gamma = 0.44)$; $(\alpha_0 = 27$ deg, $\gamma = 0.63)$ and $(\alpha_0 = 32.5$ deg, $\gamma = 0.89)$] the experiments give the same value of the thrust coefficient. This experimental value of $\tau = 0.16$ is predicted by the FWA model with a percentage error less than 0.5% at $\alpha_0 = 32.5$ deg, less than 1% at $\alpha_0 = 27$ deg, and less than 2% at $\alpha_0 = 23\%$, respectively, as shown in Fig. 8.

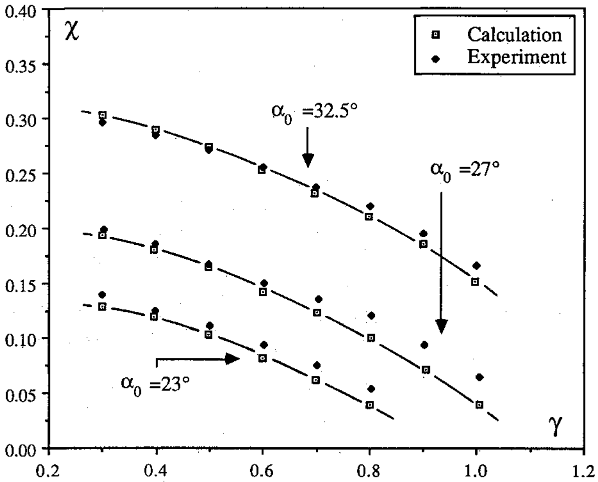

Fig. 9 Comparison of calculation and experiment on the power coefficient $\chi = \chi(\gamma)$.

The calculations of the power coefficient χ also show a good agreement with experimental data in Fig. 9. For $\gamma \geq 0.7$ and $\alpha_0 \leq 27$ deg, the predicted value is shown to slightly underestimate the experiment. This can be attributed to the fact that in the present FWA calculations no Reynolds-number correction is introduced on the airfoil characteristics (C_L, C_D), which are given as input data of the model at a fixed Reynolds number (see Fig. 7). When γ increases above 0.7, this Reynolds number (about 10^6) becomes five times higher than the actual Reynolds number of the experiments. Therefore, the sensitivity of the C_D coefficient on Reynolds-number influence is responsible for the slight theoretical underestimation observed in Fig. 9 on the power coefficient. Similar satisfactory comparisons between calculation and experiment are also obtained on the propeller efficiency $(\eta = \gamma\tau/\chi)$, as it can be deduced from the results presented in Figs. 8 and 9. Moreover, it should be emphasized that the present comparisons between calculation and experiment on the overall performances (τ, χ, η) as a function of α_0 and γ has been possible because no change on the pitch-angle value α_0 is needed during the present FWA convergence procedure. As discussed in Refs. 12–14, such comparisons become questionable when an increase of the pitch angle is required to match the thrust coefficient and converge the FWA iterative process.

Concerning the local instantaneous velocity field induced in the wake, the comparisons between calculation and experiment have been done for several planes $Z/R =$ const downstream of the propeller. The value selected in Figs. 10a–10c corresponds to an axial distance close to the blades $(Z/R = 0.203)$. The radial, tangential, and axial components $\bar{U}, \bar{V}, \bar{W}$ are plotted vs the reduced blade radius ξ at different values of the blade azimuth ψ, for the case $\alpha_0 = 32.5$ deg and $\gamma = 0.89$. In Figs. 10a–10c, the tip vortex trace on the fixed downstream plane $Z/R = 0.203$ is localized at $r_t/R = 0.97$ and $\psi_t = 37$ deg. The calculated velocity profiles obtained at $\psi = 15$, 35, 45, and 75 deg are shown to be in good agreement with experiments for all of these azimuths, even those that are very close to the tip vortex passage ($\psi = 35$ and 45 deg).

The velocity disturbance observed on each $\bar{U}, \bar{V}, \bar{W}$ velocity component is typical of the vortex influence and is well predicted by the FWA calculation model. Similar good results are also obtained at a larger axial distance from the rotating

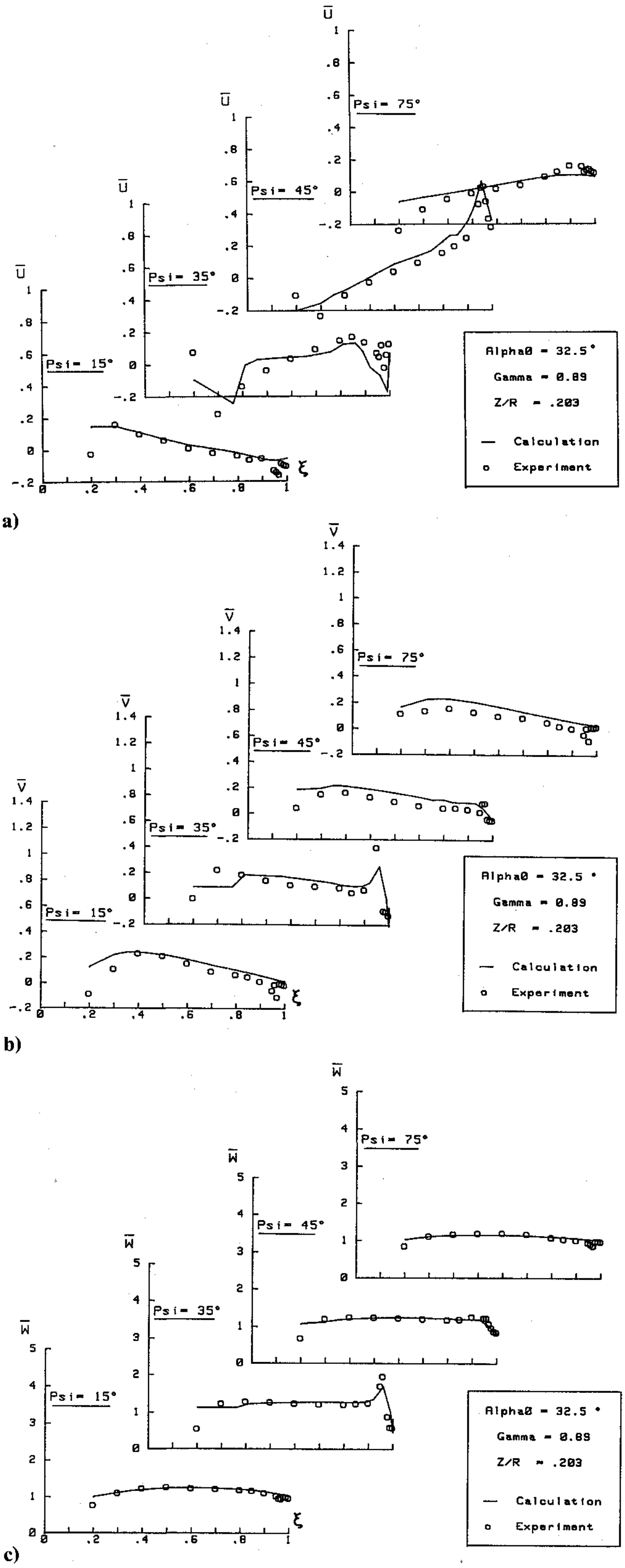

Fig. 10 Comparison of calculation and experiment on the instantaneous three-dimensional velocity field as a function of ξ and at azimuths $\psi = 15, 35, 45$, and 75 deg: a) $\bar{U}$ component: b) $\bar{V}$ component; and c) $\bar{W}$ component.

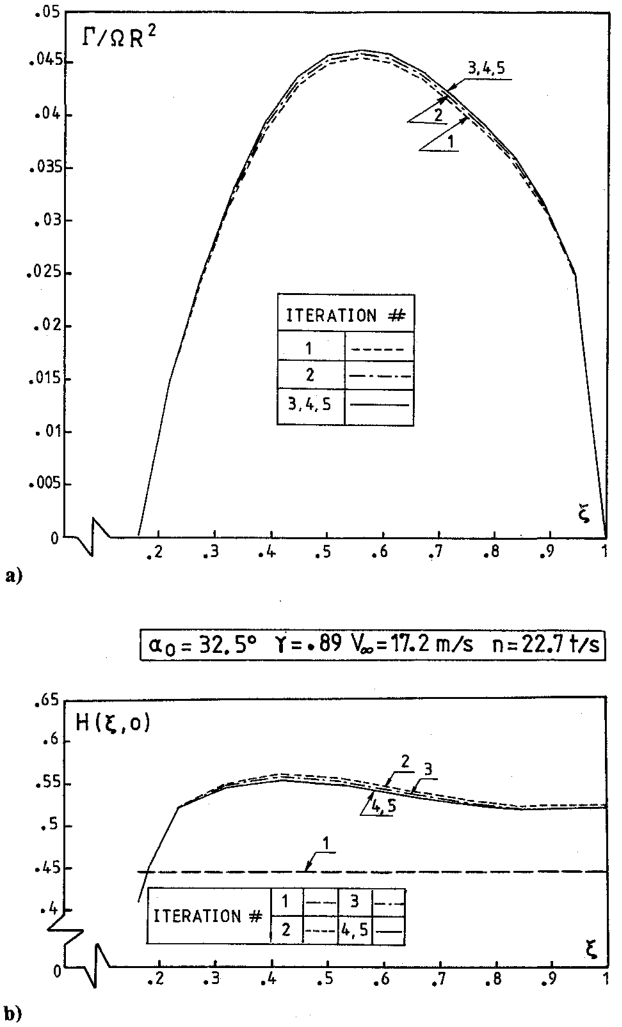

Fig. 11 Converged solution as a function of number of iterations: a) blade circulation, and b) pitch of the vortex-sheet filaments.

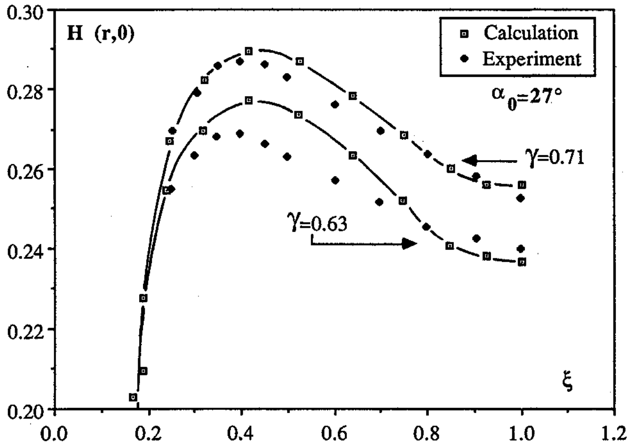

Fig. 12 Comparison of calculation and experiment on the pitch of the vortex-sheet filaments at $\psi = 0$ deg for $\alpha_0 = 27$ deg.

plane when using the preceding far-wake representation and the finite-vortex core model in the vicinity of the singularity.

Moreover, it should be noticed that the number of iterations required to converge the equilibrium procedure (step 1 in Fig. 7) never exceeded 5 iterations for all of the calculations presented in this study for the propeller axial flight. As an example, Figs. 11a and 11b give the blade circulation $\Gamma = \Gamma(\xi)$ and the pitch of the inboard vortex lines at $\psi = 0$ deg on the blade $H(\xi,0)$ calculated at the successive iteration steps for the pair of operating parameters ($\alpha_0 = 32.5$ deg; $\gamma = 0.89$). As shown in this figure, the fifth iteration presents a converged solution on the vortex-sheet position ($\xi < 10^{-4}$), which is

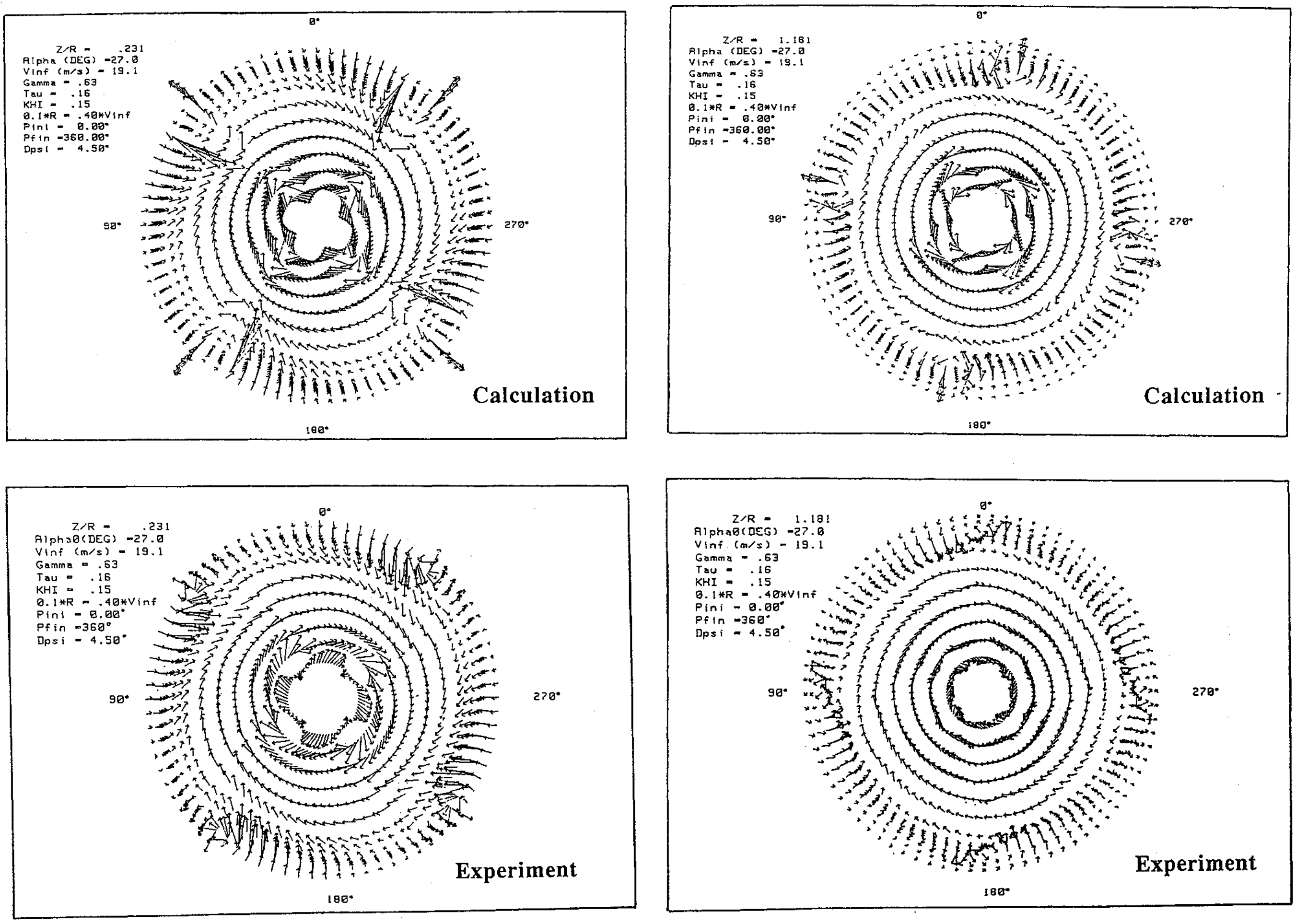

a) $Z/R = 0.231$ b) $Z/R = 1.181$

Fig. 13 Comparison of calculation and experiment on the resultant radial velocity flowfield for $\alpha_0 = 27$ deg.

obtained in this case with $N_P = 11$ and $N_L = 12$. Although the number of iterations is reduced, the present equilibrium procedure provides a converged solution on the vortex-sheet position that compares well with the experiments. An example of comparison calculation/experiment on the pitch $H(\xi,0)$ of the inboard vortex-sheet filaments is given in Fig. 12 for $\alpha_0 = 27$ deg and two values of the operating parameter $\gamma = 0.63$ and $\gamma = 0.71$. At all of the points on the blade, the FWA-model results show a good agreement with the data deduced from the flow-visualization technique previously described (see Fig. 4). The agreement appears to be better for the higher value of the operating parameter at $\gamma = 0.71$.

After the equilibrium procedure is converged for a given pair of parameters (α_o, γ), the complete overall performances and the local three-dimensional velocity field at any point in the wake can be additionally obtained (see Fig. 7) within a very short computing time requirement.

As exemplified in Figs. 13a and 13b, a fine description of the induced radial velocity field can be calculated at several downstream distances in the wake. Each of these maps represents the complete radial flowfield ($0 \text{ deg} \leq \psi \leq 360 \text{ deg}$) calculated and measured at two different axial distances $Z/R = 0.231$ and 1.181 behind the propeller operating at $\alpha_0 = 27$ deg and $\gamma = 0.63$. Maps of the two components (U_r, V_r) of the resultant radial velocity are deduced from the velocities $U = U(\xi,\psi)$ and $V = V(\xi,\psi)$ using the expressions

$$U_r = U \cos\psi + V \sin\psi \qquad V_r = V \cos\psi - U \sin\psi \quad (10)$$

The resultant velocity vector $(U_r^2 + V_r^2)^{1/2}$ is then represented at 80 different phases of the period with a step azimuth of 4.5 deg. At a given blade position ψ, the radial velocity is plotted along 15 blade radii ranging from the hub ($\xi = 0.165$) to the tip ($\xi = 1$). In the plots, a velocity vector represented by an arrow of $0.1R$ length is equal to $0.4V_\infty$.

Using such flow map representations, the four blades can be considered as fixed at the four principal azimuths ($\psi = 0$, 90, 180, and 270 deg), and the wake shed from each blade develops and rotates counterclockwise as Z/R increases. As shown in Figs. 13a and 13b, the FWA calculation provides a detailed radial flowfield that is in good agreement with experiments all along the Z direction. At a given $Z/R = \text{const}$, the radial wake contraction, the tip vortex imprint on the Z plane, as well as the neutral flow zone delimiting the respective influences of the hub and the tip vortex, are shown to be very similar on the calculated and measured flow maps. As Z/R increases, the neutral zone located in the middle blade region expands rapidly. The corresponding reduction of the influence of the blade tip and hub is also well predicted by the present FWA calculation model. The major discrepancies between calculation and experiment are observed in the blade-root region where the FWA model generally overestimates the experimental flowfield. Further improvements in the model could be achieved by including the nonpenetration flow condition and the adequate hub geometry in this blade-root region.

From the previous radial velocity field joint to the corresponding axial velocity field obtained at the different downstream Z planes, it has been possible to synthesize the complete evolution of the whole vortex-sheet geometry issued from one blade and developing until the far-wake instabilities are reached. Figures 14a and 14b present the calculated vortex-sheet geometry associated with the blade for two

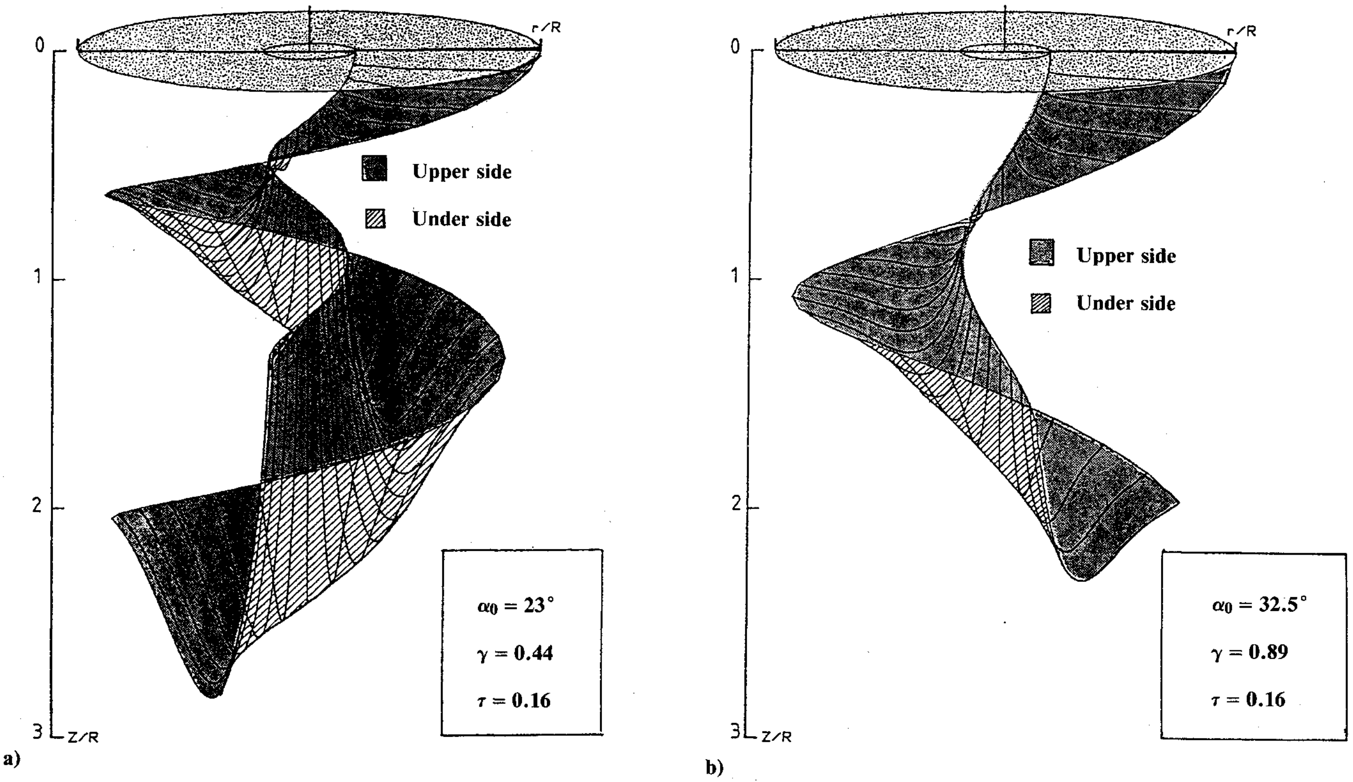

Fig. 14 Calculated vortex-sheet geometry shed from one blade at $\tau = 0.16$: a) $\alpha_o = 23$ deg, $\gamma = 0.44$; and b) $\alpha_0 = 32.5$ deg, $\gamma = 0.89$.

different operating conditions ($\alpha_0 = 23$ deg; $\gamma = 0.44$) and ($\alpha_0 = 32.5$ deg; $\gamma = 0.89$) selected so that the thrust coefficient remains constant at $\tau = 0.16$. Figure 14 gives a side view of the rotating plane tilted with a yaw angle of 10 deg. The upper side of the vortex sheet is represented by the shaded regions, whereas the hatched regions correspond to the under side. Although the thrust coefficient remains constant in both cases, the FWA calculations clearly show the development of quite different vortex-sheet geometries for the present axial flight regime. It should be noticed that in the hovering rotor case, a unique prescribed wake geometry was obtained when the pitch angle and the thrust coefficient are given (see Refs. 1–3).

Based on the aforementioned calculation results concerning the three-dimensional velocity field and the associated vortex-sheet geometry, it can be concluded that the present FWA model provides a realistic wake-flow description that appears to be sufficiently detailed for use in the investigation of more complex aerodynamic interference problems between the propeller wake and the downstream aircraft components.

Conclusions

In the present study, numerical and experimental approaches have been derived to investigate the isolated propeller aerodynamic field over a wide range of parameters of the axial flight regime. Extensive measurements of overall thrust and torque coefficients, tip vortex paths, and three-dimensional instantaneous velocity field have been performed at different propeller operating conditions, in order to constitute a complete and reliable data base for both elaboration and evaluation of the numerical approach. Concerning the tip vortex paths and the azimuthal far-wake positions, measurements have been synthesized according to an empirical formulation. Although this empirical formulation presents a form similar to those derived for the hovering flight case (with $V_\infty = 0$), it is shown to be strongly dependent on the upstream parametric conditions α_0 and γ. The present empirical formulation accounts for this dependence.

The numerical approach has been based on an FWA method that uses a new complete equilibrium procedure on both the tip vortex line and the inboard vortex-sheet filaments. Semi-infinite vortex cylinders have been used to model the far-wake region positioned at the azimuth ψ_s given by the empirical formulation. The present comparisons between calculation and experiment have demonstrated the good efficiency of the FWA model to predict both the overall and local aerodynamic fields of the propeller in axial flight. Good agreement between calculated and measured quantities has been shown on the thrust and power coefficients, the radial and axial velocity fields in the near- and far-wake regions, as well as the complete vortex-sheet geometry (pitch and distortion). However, further improvements in the model could be achieved by including 1) an adequate hub geometry model accounting for the flow near the blade-root region where the largest deviations between experiment and calculation are observed; and 2) a Reynolds-number correction to improve the power-coefficient prediction at certain operating parameters of the propeller.

Additionally, the present results have shown that the complete equilibrium procedure in axial flight is no more time consuming than those limited to the tip vortex line alone in the hovering flight case. Finally, this study also indicates that the present FWA method, which provides a realistic and detailed wake-flow description, can be suitable to investigate more complex aerodynamic interference phenomena between the propeller wake and the near aircraft components.

Acknowledgment

The authors gratefully acknowledge the support provided by the Direction des Recherches, Etudes et Techniques under Grants 85/115 and 87/095.

References

[1]Johnson, W., Lau, B. H., and Bowles, J. V., "Calculated Performance, Stability, and Maneuverability of High-Speed Tilting-Prop-Rotor Aircraft," *Proceedings of the 12th European Rotorcraft Forum*, Paper No. 15, Garmisch-Partenkirchen, Sept. 1986, pp. 15.1–15.12.

[2]Landgrebe, A. J., "The Wake Geometry of a Hovering Helicopter Rotor Performance," *Journal of the American Helicopter Society*, Vol. 17, No. 4, Oct. 1972, pp. 3–15.

[3]Kocurek, J. D. and Tangler, J. L., "A Prescribed Wake Lifting

Surface Hover Performance Analysis," *Journal of the American Helicopter Society*, Vol. 22, No. 11, Jan. 1977, pp. 24–35.

[4] Egolf, T. A. and Landgrebe, A. J., "Helicopter Rotor Wake Geometry and Its Influence in Forward Flight," NASA CR 3726 and 3727, Vols. I and II, June 1983.

[5] Elliott, J. W., Althoff, S. L., Sellers, W. L., and Nichols, C. E., "Inflow Velocity Measurements Made on an Helicopter Rotor Using a Two-Component Laser Velocimeter," AIAA Paper 87-1321, June 1987.

[6] Favier, D. and Maresca, C., "Etude du Sillage 3D d'une Hélice Aérienne Quadripale," AGARD-FDP on Aerodynamics and Acoustics of Propellers, CP-366, Paper No. 15, Oct. 1984.

[7] Nsi Mba, M., Meylan, C., Maresca, C., and Favier, D., "Radial Distribution Circulation of a Rotor in Hover Measured by Laser Velocimeter," *Proceedings of the 10th European Rotorcraft Forum*, Paper No. 12, The Hague, Aug. 1984, pp. 12.1–12.18.

[8] Summa, J. M. and Clark, D. R., "A Lifting Surface Method for Hover/Climb Airloads," *Proceedings of the 35th Annual American Helicopter Society Forum*, Washington, D.C., May 1979.

[9] Caradonna, F. X. and Tung, C., "Experimental and Analytical Studies of a Model Helicopter Rotor in Hover," *Vertica*, Vol. 5, No. 2, May 1981, pp. 149–161.

[10] Maresca, C., Nsi Mba, M., and Favier, D., "Prédiction et Vérification Expérimentale du Champ des Vitesses d'un Rotor en Vol Stationnaire," AGARD-FDP on Aerodynamics Loads on Rotorcraft, CP-334, Paper No. 7, May 1982.

[11] Bliss, D. B., Teske, M. E., and Quackenbush, T. R., "Free-Wake Calculations Using Curved Vortex Elements," *Proceedings of 1st International Conference on Rotor Basic Research*, Research Triangle Park, NC, Feb. 1985, pp. 1–22.

[12] Maresca, C., Favier, D., and Nsi Mba, M., "A Prescribed Radial Circulation Distribution of a Hovering Rotor Blade," *Proceedings of the 12th European Rotorcraft Forum*, Paper No. 23, Garmisch-Partenkirchen, Sept. 1986, pp. 23.1–23.25.

[13] Johnson, W., "Recent Developments in Rotary Wing Aerodynamic Theory," *AIAA Journal*, Vol. 24, Aug. 1986, pp. 1219-1244.

[14] Landgrebe, A. J., "Overview of Helicopter Wake and Airloads Technology," *Proceedings of 12th European Rotorcraft Forum*, Paper No. 18, Garmisch-Partenkirchen, Sept. 1986, pp. 18.1–18.21.

[15] Chen, C. S., Velkoff, H. R., and Tung, C., "Free-Wake Analysis of a Rotor in Hover," AIAA Paper 87-1245, June 1987.

[16] Favier, D., Nsi Mba, M., Barbi, C., and Maresca, C., "A Free-Wake Analysis for Hovering Rotors and Advancing Propellers," *Proceedings of the 11th European Rotorcraft Forum*, Paper No. 21, London, Sept. 1985; see also *Vertica*, Vol. 11, March 1987, pp. 493–511.

[17] Martin, R. M., Elliott, J. W., and Hoad, D. R., "Experimental and Analytical Predictions of Rotor Blade–Vortex Interaction," *Journal of the American Helicopter Society*, Vol. 31, No. 4, Oct. 1986, pp. 13–20.

[18] Srinivasan, G. R., McCroskey, W. J., and Baeder, J. D., "Aerodynamics of Two-Dimensional Blade–Vortex Interaction," AIAA Paper 85-1560, July 1985.

[19] Ettaouil, A., "Etude Numérique du Champ Aérodynamique d'une Hélice Aérienne Isolée ou en Interaction avec une Voilure—Validation par Comparaison Avec l'Expérience," Thèse de Doctorat, Université d'Aix-Marseille II, Institut de Mécanique des Fluides, Sept. 1987.